ACS SENSORS

Article

Cite This: ACS Sens. 2018, 3, 1093−1101

pubs.acs.org/acssensors

Ferromagnetic Resonance Biosensor for Homogeneous and Volumetric Detection of DNA

Bo Tian, Xiaoqi Liao, Peter Svedlindh, Mattias Strömberg,* and Erik Wetterskog*

Department of Engineering Sciences, Uppsala University, The Ångström Laboratory, Box 534, SE-751 21 Uppsala, Sweden

Supporting Information

ABSTRACT: The ability to detect and analyze the state of magnetic labels with high sensitivity is of crucial importance for developing magnetic biosensors. In this work, we demonstrate, for the first time, a ferromagnetic resonance (FMR) based homogeneous and volumetric biosensor for magnetic label detection. Two different isothermal amplification methods, i.e., rolling circle amplification (RCA) and loop-mediated isothermal amplification (LAMP), are adopted and combined with a standard electron paramagnetic resonance (EPR) spectrometer for FMR biosensing. For the RCA-based FMR biosensor, binding of RCA products of a synthetic *Vibrio cholerae* target DNA sequence gives rise to the formation of aggregates of magnetic nanoparticles. Immobilization of nanoparticles within the aggregates leads to a decrease of the net anisotropy of the system and a concomitant increase of the resonance field. A limit of detection of 1 pM is obtained with a linear detection range between 7.8 and 250 pM. For the LAMP-based sensing, a synthetic Zika virus target oligonucleotide is amplified and detected in 20% serum samples. Immobilization of magnetic nanoparticles is induced by their coprecipitation with $Mg_2P_2O_7$ (a byproduct of LAMP) and provides a detection sensitivity of 100 aM. The fast measurement, high sensitivity, and miniaturization potential of the proposed FMR biosensing technology makes it a promising candidate for designing future point-of-care devices.

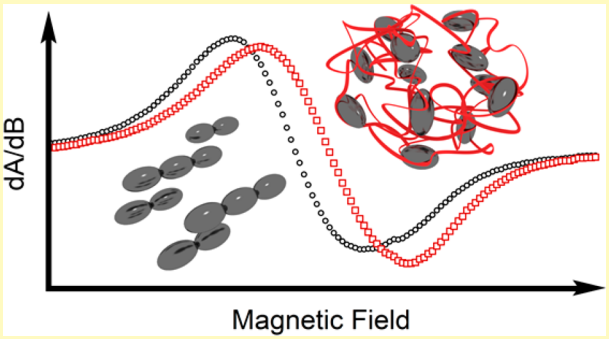

KEYWORDS: *ferromagnetic resonance, magnetic nanoparticles, homogeneous detection, volumetric detection, rolling circle amplification, loop-mediated isothermal amplification*

Homogeneous biosensor strategies benefit greatly from simple "mix and measure" protocols leading to short total assay times, a high degree of user friendliness, a low risk of contamination, and the potential for automation, which are all desirable properties for in situ decentralized diagnostics.[1,2] The combination of volumetric sensing methods and homogeneous biosensor strategies is typically robust, simple, and has the advantage of relying on signal generation from the entire suspension volume. Particularly, in combination with the large surface area and unique properties of nanoparticle labels, they are of great interest for point-of-care diagnostic applications.[3,4] Among the variety of different homogeneous and volumetric biosensors, magnetic nanoparticle (MNP) based systems are particularly promising due to their biocompatibility, high chemical stability, and low background signal (typical biological matrices are nonmagnetic).[5,6] Also, due to the intrinsic properties of MNPs, they have great potential for imaging (such as magnetic resonance imaging[7] and magnetic particle imaging[8]) and other in vivo applications (such as drug delivery[9] and hyperthermia[10]), all closely related to MNP based sensing methods. However, the number of readout methods available for homogeneous and volumetric magnetic biosensing are quite limited and include, e.g., superconducting quantum interference device (SQUID) magnetometry,[11,12] magnetic susceptometry,[13,14] nuclear magnetic resonance (NMR),[15,16] and optomagnetic sensing.[17,18] Additionally, requirements of, e.g., cryogenic coolants and/or strong homogeneous magnetic fields limit the prospects of using some of these methods for point-of-care testing.

In contrast to NMR, which probes the magnetic moment of atomic nuclei, the electron paramagnetic resonance (EPR) technique is sensitive to the physiochemical state of unpaired electrons. As such, it is widely used for studying reactions of radicals and transition metal centers. Moreover, EPR is used to study magnetic anisotropy in single crystals,[19] thin films,[20] and nanoparticles[21−23] under the acronym FMR (ferromagnetic resonance). In a field-swept EPR/FMR cavity measurement, the sample is placed in the electric field nodal, but at a maximum in the magnetic field of a standing microwave. The microwave absorption is then measured as a static magnetic field is swept through the resonance of the sample. Simply put, absorption in FMR occurs when the precession frequency of the sample magnetization matches that of the cavity microwave field. As a result of the use of a superimposed, low amplitude,

Received: January 15, 2018
Accepted: May 31, 2018
Published: May 31, 2018

DOI: 10.1021/acssensors.8b00048
ACS Sens. 2018, 3, 1093−1101

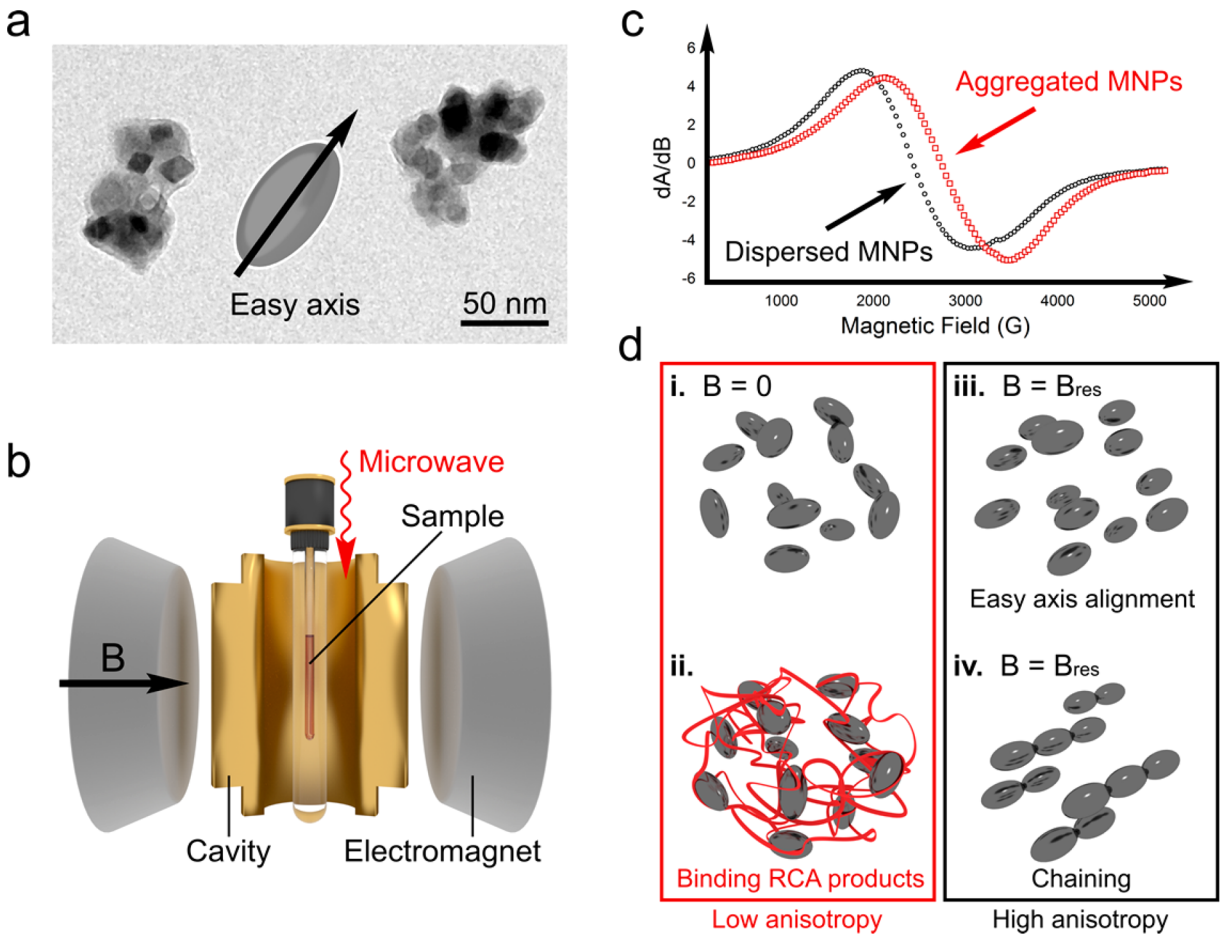

Figure 1. FMR biosensor for homogeneous and volumetric detection of DNA. (a) TEM micrograph of the BNF-100 multicore particles. The indicated easy axis of magnetization for individual particles (favorable direction of spontaneous particle magnetization) is determined by the particle shape (the long direction of the particle). (b) Sketch of the EPR cavity and magnet used for FMR sensing. (c) Typical FMR spectra of dispersed MNPs (black circles) and aggregated MNPs (red squares) in suspension. (d) Schematic illustration of the FMR biosensor: (i) MNPs are randomly oriented in suspension at $B = 0$, but align (iii) and form chains (iv) as the magnetic field is swept over the sample, resulting in a system with a high anisotropy; RCA induced aggregation (ii) immobilizes the MNPs and lowers the net anisotropy of the system.

low frequency magnetic field and a lock-in amplifier, the data recorded is typically the magnetic field derivative of the microwave absorption (dA/dB). In FMR, the principal quantity of interest is the zero-crossing of the signal, also known as the ferromagnetic resonance field (B_{res}). In ferromagnetic materials, B_{res} varies with the net magnetic (shape-, magnetocrystalline-) anisotropy of the system.[24,25] Herein, we demonstrate that it is possible to study the binding of biomacromolecules to magnetic labels using FMR, by monitoring the shift of the ferromagnetic resonance field (ΔB_{res}).

The FMR method offers high sensitivity and short measurement times and has been used for the study of fundamental properties of MNPs,[26−29] imaging,[30−33] and surface-based sensing/biosensing.[34−37] On-chip FMR sensors/biosensors can detect nano- to micron-sized magnetic particles immobilized on a small sensing area, but have up to now not been reported for practical biosensing of any real biological interactions. In this work, we demonstrate for the first time a homogeneous and volumetric biosensor for DNA detection based on FMR by probing the state of MNPs. First, we study the linear FMR detection range for unbound MNPs to investigate the sensing capability of FMR and to choose a suitable MNP concentration range for biosensing. Then we demonstrate a proof-of-concept of an RCA-based biosensing platform by monitoring MNP aggregates formed in the presence of RCA products of different lengths or concentrations. Finally, the versatility, robustness, and specificity of the proposed FMR-based biosensing principle are extended by employing loop-mediated isothermal amplification (LAMP) in addition to RCA.

EXPERIMENTAL SECTION

Conjugation of Detection Probes to MNPs. Streptavidin modified 100 nm MNPs (product 10−19−102, micromod Partikeltechnologie GmbH, Germany) were washed twice and resuspended in 1× PBS before conjugation. Biotinylated *V. cholerae* detection probes (10 μM) and MNPs (10 mg/mL) were mixed in a volumetric ratio of 1:8 followed by incubation at room temperature for 30 min. Thereafter the MNPs were washed twice using a magnetic separation stand and resuspended at a concentration of 4 mg/mL in PBS.

Rolling Circle Amplification and Hybridization of MNPs to Amplification Products. The ligation mixture (100 μL, 20 nM) for RCA was prepared by mixing 10 μL of 10× φ29 buffer, 5 μL of ATP (20 mM), 2 μL of padlock probe (1 μM), 6 μL of target DNA sequence (1 μM), 2 μL of T4 ligase (1 U/μL, Thermo Fisher Scientific), and 75 μL of Milli-Q water, followed by incubation at 37 °C for 15 min. RCA reaction mixture (30 μL) was prepared by mixing 10 μL of ligation mix (20 nM), 3 μL of 10× φ29 buffer, 2 μL of dNTPs (2.5 mM), 3 μL of BSA (2 μg/μL), 1 μL of φ29 polymerase (10 U/μL, Thermo Fisher Scientific), and 11 μL of Milli-Q water,

DOI: 10.1021/acssensors.8b00048
ACS Sens. 2018, 3, 1093−1101

followed by incubation at 37 °C for 40 min and thereafter inactivation at 65 °C for 5 min. After that, the RCA reaction mixture (30 μL) was mixed with 20 μL of hybridization buffer (0.1 M Tris-HCl pH 8.0, 0.1 M EDTA, 0.5% Tween-20 and 2.5 M NaCl) to obtain a 4 nM DNA coil solution. The solution was further diluted with hybridization buffer to obtain different concentrations of RCA products. Solutions containing RCA products were mixed with detection probe-conjugated MNPs in a volumetric ratio of 19:1 (the final concentration of MNP was around 0.15 mg/mL), followed by hybridization at 55 °C for 20 min to form MNP aggregates. DNA templates and probes used for RCA were synthesized by Biomers (Ulm, Germany), and their sequences are listed in Table S1. Three independent samples, referred to as replicates below, were prepared for each target concentration, i.e., the targets in each of these three samples were amplified separately for the following FMR measurement.

Loop-Mediated Isothermal Amplification. For primer design, a 230 bp highly conserved region from the RNA-dependent-RNA-polymerase (NS5) sequence of Zika virus was chosen as the target gene. LAMP primers were designed using Primer Explorer version 4 (https://primerexplorer.jp/e/). Four types of synthetic NS5 gene from relevant viruses were detected for specificity study: Dengue virus, GenBank EF595819; Yellow fever virus, GenBank AY541441; Japanese encephalitis virus, GenBank FJ515937; and West Nile virus, GenBank AY187015. DNA templates and primers used for LAMP were synthesized by Biomers, and their sequences are listed in Table S2. DNA samples were diluted in 1× PBS or 1× PBS containing 20% fetal bovine serum (purchased from Sigma-Aldrich, St. Louis, USA) before LAMP. The LAMP reaction mixture (100 μL) contained 0.24 mg/mL of magnetic nanoflowers (nonfunctionalized, synomag-D, product 104−00−501, micromod Partikeltechnologie GmbH), 1.6 μM of inner primers, 0.2 μM of outer primers, 0.4 μM of loop primers, 1× isothermal amplification buffer II (containing 2 mM of $MgSO_4$), 6 mM of $MgSO_4$ (8 mM in total), 32 U of *Bst* 3.0 polymerase (New England Biolabs, Ipswich, UK), 1.4 mM of dNTPs, and 40 μL of analyte solution. The mixture was incubated at 69 °C for LAMP. Three independent samples, referred to as replicates below, were prepared for each target concentration, i.e., the targets in each of these three samples were amplified separately for the following FMR measurement.

FMR Measurement. FMR measurements were performed on a Bruker ELEXSYS-E580 EPR spectrometer equipped with a standard X-band (9.47 GHz) cavity. Ten microliters of suspension (containing RCA products and MNPs) was transferred into a quartz capillary (CM Scientific, ID = 0.7 mm) using a long steel-tipped glass syringe (Hamilton-701 N) and placed in a standard EPR tube. Measurements were performed at the same height in the cavity, with 10 μL being sufficient to fill the entire active volume of the cavity (18 mm). The field was swept over a field range of 15−8000 G, using 1024 data points in one pass, taking B_{res} as the zero-crossing of the derivative of the microwave absorption (dA/dB). The offset was manually adjusted to 0 using the signal obtained in the field range of 6000−8000 G, and the data around the zero-crossing was fitted using linear regression to extract B_{res}.

RESULTS AND DISCUSSION

Working Principle of RCA-Based FMR Biosensing. The detection strategy for the target DNA is based on an isothermal DNA amplification followed by hybridizing detection probe-conjugated BNF-100 MNPs (D_h = 120 nm)[38] to the amplification products. The BNF-100 multicore particles consist of multiple Fe_3O_4 nanocrystals aggregated in a streptavidin functionalized starch shell (see Figure 1a, where the easy axis indicates the energetically favorable direction of the nanoparticle magnetic moment). The isothermal DNA amplification employed here, namely, RCA, produces long single-stranded DNA coils with tandem repeating sequences that can be recognized by the detection probe and results in aggregation of the probe-conjugated MNPs. Measurements were performed on an EPR spectrometer (as indicated in Figure 1b).

Figure 1c compares the FMR spectra of dispersed particles and aggregated particles in suspension, and clearly shows that B_{res} increases for the RCA aggregated system, relative to the nonaggregated MNPs. This phenomenon is similar to our previous observations of ferromagnetic resonance shifts in immobilized magnetic nanocluster suspensions, caused by freezing of the surrounding matrix or absorption of the MNPs in, e.g., cotton wool.[29] The differences in B_{res} reflect a difference of the induced net magnetic anisotropy of the system as the magnetic field is swept through the sample resonance field during the measurement.[26] In theory, B_{res} of a magnetic nanoparticle system can be found by solving the Smit-Beljers equation[19] for the full magnetic energy of the system. For a typical nanoparticle system, the magnetic energy is equal to the sum of the Zeeman energy, the magnetostatic self-energy (shape anisotropy), the magnetocrystalline anisotropy energy, and the dipolar interaction energy.[25] Moreover, the random orientation of the constituent crystals of the BNF-100 multicore particles (see Figure 1a) indicates that their magnetocrystalline anisotropy energy surface is at first approximation isotropic and does not contribute to the shift of B_{res}. Instead, we may, by exclusion, assign the origin of the magnetic anisotropy of the individual BNF-100 multicore particles to an effective shape anisotropy resulting from a slight elongation of the multicore particles *and/or* from chain formation (see Figure 1a).[29] Assuming only shape anisotropy and using the simplifying assumption that the magnetization vector follows the applied field yields the following resonance condition.[27,29]

$$B_{res} = B_{iso} - B_{uni}\left(1 - \frac{3}{2}\sin^2\theta\right)$$

Here, $B_{uni} = MN_{eff}$ and N_{eff} is the effective demagnetization factor. $B_{iso} = \omega/\gamma$ is the free electron resonance field ($\omega = 2\pi \times 9.47 \times 10^9$ rad s^{-1}, $\gamma = 1.76 \times 10^7$ rad s^{-1} G^{-1}); θ is the angle between the anisotropy axis and the magnetization vector. For the resonance field of a fully aligned dispersion oriented along the field axis ($\theta = 0$) we have $B_{res} = B_{iso} - B_{uni}$. Conversely, for the aggregated RCA system with randomly aligned easy axes, $\sin^2\theta = \frac{2}{3}$ and $B_{res} = B_{iso}$. We can make a rough estimate of B_{uni} assuming that the BNF-100 particles have the shape of prolate ellipsoids with semiaxes $a > b = c$ and calculate the demagnetization tensor using Osborn's formulas.[39] This results in an effective demagnetization factor of $N_{eff} = N_\perp - N_\parallel$, with $N_{xx} = N_{yy} = N_\perp > N_\parallel = N_{zz}$. Assuming a MNP elongation in the range of c/a = 1.1−1.5 ($N_{eff}/4\pi \approx 0.04$−$0.15$) and a saturation magnetization of 370 emu/cm^3 yield a maximum shift of the resonance field in the range of $\Delta B_{res} = -B_{uni}$ = 170−700 G for the aligned MNPs.[40] These ΔB_{res} values appear to be in the range of the experimentally observed resonance shifts. We would like to point out that the immobilization of multicore particles inside RCA products in a field of B_{res} would only be partial, while the MNPs inside the "soft" RCA aggregates (cf., Figure 1d) can be expected to retain some rotational mobility. Moreover, the BNF-100 particles show a clear signature of magnetic field-induced chain formation, evidenced by the decrease of B_{res} with increasing MNP concentration (studied over the range of 10 μg/mL to 2.5 mg/mL, see Figure S1). Chaining, in contrast to rotational alignment of the MNPs, depends on particle concentration, as well as on the effective

DOI: 10.1021/acssensors.8b00048
ACS Sens. 2018, 3, 1093−1101

moment of the particles.[41−43] Chain formation of the BNF-100 particles can also be observed directly in the light microscope when a field of 1000 G magnetic field is applied over a thin liquid layer of MNP dispersion (Figure S2). In contrast, we observed a negligible decrease of B_{res} with increasing concentration in the case of smaller (D_h = 56 nm) synomag-D nanoflowers used in the LAMP study (vide infra) and no visible indication of chain formation in the light microscope (Figures S1 and S2). Charilaou et al. demonstrated that the effect of chaining with respect to B_{res} can be calculated by explicitly calculating the dipolar energy of the assembled chain or alternatively approximated by an additional contribution to the magnetic shape anisotropy.[25] In conclusion, we argue that the experimentally observed shift in B_{res} reflects a change of the net magnetic anisotropy of the system as the magnetic field is swept over the sample. The resulting shift (ΔB_{res}) is the result at least one of two dynamic effects, illustrated in Figure 1d: (1) the alignment of the easy axes of the individual MNPs,[44] and (2) chaining of MNPs due to dipolar interactions (increasing the effective shape anisotropy of the system).[25] Currently, more work is needed to disentangle these effects; both mechanisms are likely to be inhibited by RCA-induced aggregation of the MNPs and contributing to the effectiveness of the sensor, either by (rotationally) fixing the MNPs with respect to each other or by preventing them from assembling into chains. Nevertheless, ΔB_{res} provides an indirect measure of MNP aggregation, and thus of the concentration and/or length of RCA products.

Volumetric sensors measure analytical signals coming from the entire measurement volume, i.e., representing an ensemble average. Therefore, the resolving power of volumetric sensors can easily be restricted since there is no possibility to separate the unbound MNPs from the ensemble. Hence, it is difficult for volumetric sensors to distinguish a weak positive signal from a high level of background signals.[5] On the one hand, to achieve better sensitivity, a low MNP concentration is preferred in order to reduce the background signal generated by the free (noncaptured) MNPs. On the other hand, a low MNP concentration means a narrow dynamic detection range as well as a weak robustness against system disturbance. To find an optimum concentration of the 100 nm MNPs for DNA detection, we measured a series of FMR spectra (average spectra of three independent replicates, shown in Figure 2a) of MNP suspensions with concentrations ranging from 10 μg/mL to 10 mg/mL. The associated MNP concentration dependent FMR response curve defined as the positive maximum of the FMR signal (dA/dB) at 1830 G vs the concentration of MNPs is shown in Figure 2b, with a log−log plot shown in the inset. Figure 2b shows that the amplitude of the FMR signal varies linearly with the MNP concentration over 3 orders of magnitude, and that the setup is sensitive enough for the detection of MNP concentrations down to 10 μg/mL. To balance the MNP detection sensitivity with reliability and dynamic detection range, we chose a MNP concentration of ∼0.15 mg/mL for our further experiments.

RCA-Based DNA Quantification. In order to test the capability of the FMR technique to probe the RCA-induced MNP aggregation, we measured the FMR spectra of RCA products of different lengths by varying the RCA reaction time (0−60 min, average spectra of three independent replicates, Figure 3a). As a relevant target, we chose a synthetic DNA sequence from *Vibrio cholerae*, the causative agent of cholera. As shown in Figure 3b, RCA products of increasing lengths result in a monotonous increase of ΔB_{res}, where the baseline is

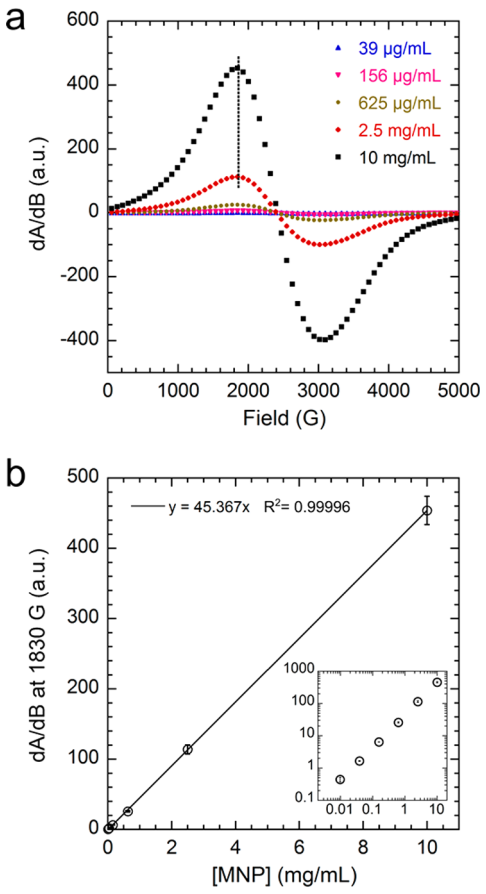

Figure 2. FMR spectra for free MNPs suspended in buffer solution at constant microwave power (a) and MNP concentration dependent FMR response curve (b) calculated as the value of dA/dB at 1830 G versus MNP concentration. The inset in (b) shows a log−log plot of the data in panel (b). The black dotted vertical line in (a) indicates the peak position at 1830 G. The black solid line in (b) indicates the linear detection range. Error bars indicate the standard deviation of three independent replicates.

defined as the average B_{res} of samples without RCA incubation, i.e., reaction time of 0 min. This confirms that longer RCA products to a higher degree inhibit chaining and alignment of the MNP easy axis, which is the energetically favorable direction of the nanoparticle magnetic moment, decreasing the net anisotropy of the MNP suspension. Indeed, longer RCA times have been shown to increase the number of binding sites, thereby trapping more MNPs. Theoretically, the length of RCA products should increase with the reaction time until the dNTPs are used up or the φ29 polymerase is denatured.[45,46] Due to the high target DNA concentration (500 pM) used here, it is evident that also short RCA products (reaction time of 10 min, red diamonds in Figure 3a) lead to a dramatic increase of ΔB_{res}. A plateau of ΔB_{res} is observed (Figure 3b) when the RCA reaction time is longer than 50 min. We have three hypotheses for explaining the ΔB_{res} saturation: (1) depletion of unbound MNPs due to an excessive number of RCA binding sites, i.e., all MNPs are bound; (2) the length increase of RCA products has negligible contribution to the hydrodynamic size of the DNA coils when the coils are large; and (3) the MNP aggregate sterically prevent the binding sites of the DNA coils from further reaction.

For the proof-of-concept, a synthetic target DNA sequence (from *V. cholerae*) was amplified by RCA and quantified by the

DOI: 10.1021/acssensors.8b00048
ACS Sens. 2018, 3, 1093−1101

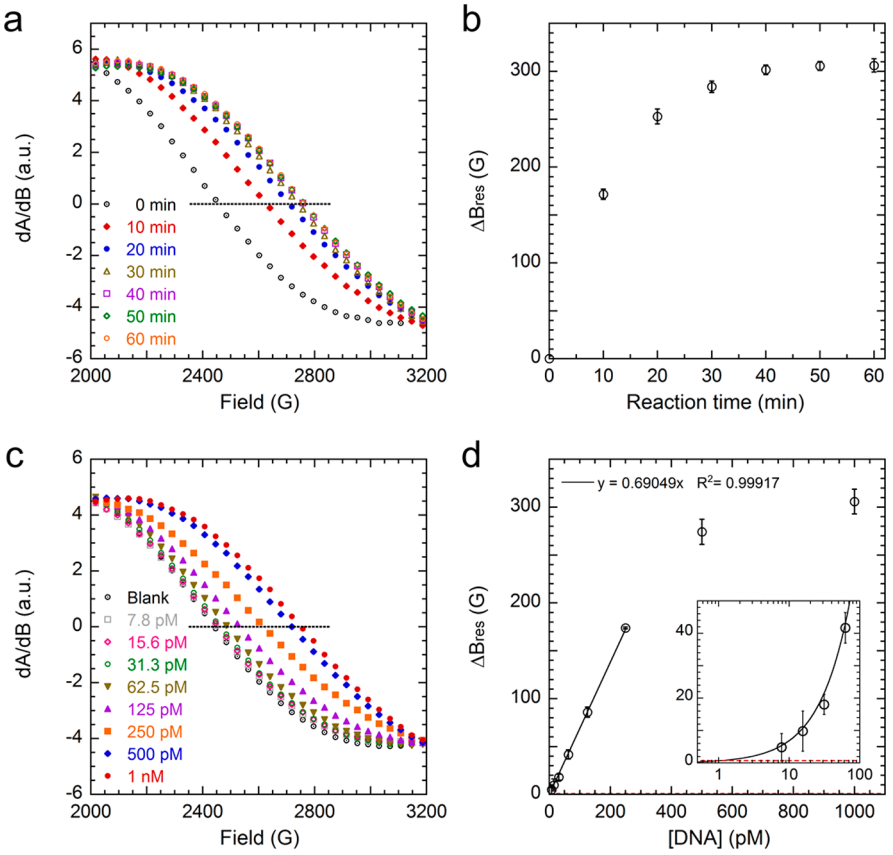

Figure 3. (a,b) FMR spectra and resonance field shift (ΔB_{res}) versus RCA reaction time. Samples containing 500 pM of the synthetic *V. cholerae* sequence are used to perform RCA with different reaction times. (c,d) FMR spectra and dose−response curve for RCA-based homogeneous and volumetric detection of the synthetic *V. cholerae* sequence. The inset in (d) shows a close-up lin-log plot of the data in panel (d). The black dotted horizontal lines in (a) and (c) indicate the zero value of dA/dB. The black solid lines and red dashed lines in (d) indicate the linear fitting and the cutoff value, respectively. Error bars indicate the standard deviation of three independent replicates.

FMR sensor. From the FMR spectra (of three independent replicates) shown in Figure 3c it can be seen that B_{res} increases monotonously with increasing target DNA concentration. Blank controls (buffer solutions) were measured for normalizing and for calculating the cutoff value, which is defined as the average B_{res} for the triplicate measurements plus three times the standard deviation of the triplicate. A linear correlation between ΔB_{res} and the target concentration can be observed between 7.8 and 250 pM. A limit of detection (LOD) of 1 pM obtained according to the 3σ criterion (the crossing point of the two lines in Figure 3d inset). Similar to the trend in Figure 3b, we observe a plateau of ΔB_{res} (but no hook effect observed) at the highest target concentrations (500 pM and 1 nM samples).

The widespread use of the RCA strategy allows for a convenient comparison between biosensors. For reported magnetic biosensors using the RCA strategy to aggregate MNPs, LODs of 2, 3, 4, and 10 pM were achieved by Hall-effect bridge sensor,[47] SQUID,[48] AC susceptometer,[49] and optomagnetic sensor,[50] respectively. As a comparison, the LOD of the proposed FMR sensor is 1 pM, thus slightly more sensitive than comparable readout methods. However, to the best of our knowledge, NMR sensors have not been combined with RCA, which means that a direct comparison between NMR and FMR sensors cannot be made. NMR-based biosensors, compared to other magnetic sensors including the FMR-based ones, are theoretically more sensitive due to their intrinsic signal amplification. NMR measures ^{1}H protons, while each MNP influences millions of ^{1}H protons of surrounding water molecules.[5] A typical NMR-based biosensor, reported by Chen et al., employed an optimum MNP concentration of 0.001 mg/mL for biosensing,[16] which is much lower than the MNP dose chosen in this work (approximately 0.15 mg/mL). Although the MNPs in these two works are not identical, a qualitative comparison of the sensitivities can still be made.

FMR-based biosensors have other advantages including the ability to rapidly (within 1 min, counted roughly as the time from placing the sample into the EPR device until getting the signal output) analyze very small sample volumes (10 μL) with high repeatability. By using magnetic nanoparticle systems with different intrinsic anisotropies and associated spectral positions (e.g., by varying the shape and composition of the MNPs), the FMR biosensor holds the potential for multiplex detection. Finally, one of the most exciting prospects of FMR based biosensing is the large potential for miniaturization of sensor units. While experiments performed in the current work were carried out on a bulky commercial EPR spectrometer, the sensor unit may be scaled down to length scales relevant for microfluidic systems (e.g., by the use of coplanar waveguides),[51,52] or even to the micron-scale using microfabricated resonators.[53,54]

Working Principle of LAMP-Based FMR Sensing. The performance of the homogeneous FMR system for DNA detection can be further improved by utilizing (1) DNA amplification strategies with a higher efficiency, and (2) MNPs with more optimal properties (e.g., higher microwave absorption and higher anisotropy). In order to take a first

DOI: 10.1021/acssensors.8b00048
ACS Sens. 2018, 3, 1093−1101

step in this direction, and to showcase the versatility of the FMR technique toward other sensing schemes, we demonstrate a time-resolved oligonucleotide detection method by combining loop-mediated isothermal amplification (LAMP) with nonfunctionalized magnetic nanoflowers[55,56] (synomag-D, D_h = 56 nm). In previous work, we used LAMP in combination with AC-susceptometry to detect nonfunctionalized magnetic labels for the sensing of a synthetic Zika oligonucleotide.[14] In FMR, synomag-D exhibits ≈ 30× higher microwave absorption (per weight Fe) than BNF-100. Within a short LAMP reaction time (≤20 min), $Mg_2P_2O_7$ (a byproduct of LAMP) coprecipitates and traps the suspended magnetic nanoflowers. The LAMP reaction suspension (containing nanoflowers and 100 fM of Zika virus oligonucleotide) was incubated at 69 °C and measured by FMR after different incubation times (Figure 4a, average spectra of three independent replicates). During the first 10 min of the LAMP reaction, no coprecipitation was observed by FMR. At the incubation time of 12 min, a part of the suspended nanoflowers was immobilized in the $Mg_2P_2O_7$ precipitate, leading to an additional negative peak at high field range (~3600 G). Quantitatively, the onset of the reaction is evidenced by a steep increase of ΔB_{res} (shown in Figure 4b) around the LAMP reaction time of 10−14 min, increasing only marginally between 14 and 16 min; as previously, the baseline is defined as the average B_{res} of the samples without LAMP incubation (0 min). Note that the immobilization of nanoflowers by coprecipitation is heterogeneous, whereas the LAMP reaction itself is homogeneous. As such, the resulting 12 min LAMP spectrum does not reflect a continuum of discrete resonance shifts. Rather, it is a superposition of two states, bound and unbound MNPs, and may be regarded as a linear combination of the 10 and 14 min LAMP spectra. The time period from the appearance of $Mg_2P_2O_7$ to the precipitation of particles is very short (usually within 30 s); therefore, the standard deviation of the replicates at the point of 12 min is much larger than that of other points. This problem can be avoided by employing a real-time sensing format, including a built-in heater to perform LAMP reaction inside the setup, instead of the current time-resolved end-point format.

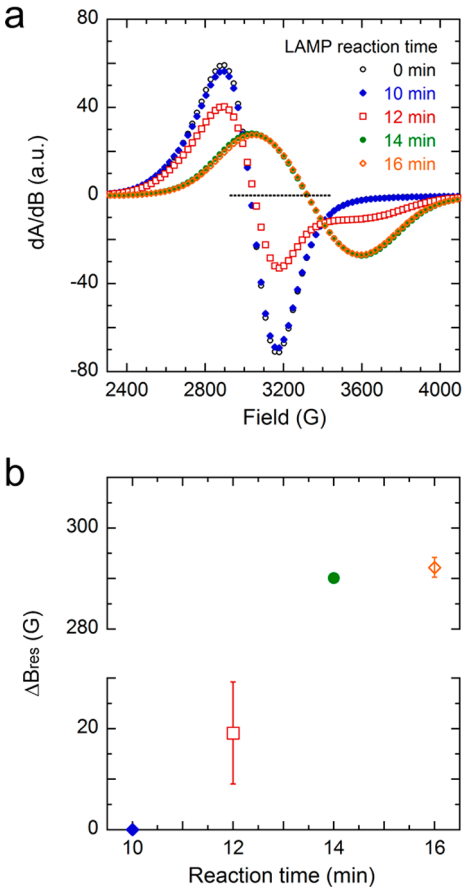

Figure 4. FMR spectra (a) and resonance field shift (ΔB_{res}) versus reaction time (b) for LAMP-based time-resolved detection of the synthetic Zika virus oligonucleotide. The concentration of Zika virus oligonucleotide is 100 fM. The black dotted horizontal line in (a) indicates the zero value of dA/dB. Error bars indicate the standard deviation of three independent replicates.

LAMP-Based DNA Quantification. In order to demonstrate the robustness of our system in biological matrixes, the following experiments were performed by measuring oligonucleotides diluted in 1× PBS containing 20% fetal bovine serum. If we consider the detection of MNPs only, serum has limited effects on the FMR signal in terms of (1) slightly increasing the viscosity of the suspension (the viscosity of 20% serum is 1.08 to 1.16 times that of water), and (2) inducing MNP aggregation due to nonspecific binding. Both of these effects can be compensated by using control samples. Other problems coming from the matrix effects of serum on biological/chemical objects/reactions are (1) inhibition of the amplification reaction (by inhibiting/digesting/binding the enzyme/target), and (2) generation of false positive results (e.g., serological cross-reactivity).

Serial dilutions of target DNA, ranging from 100 fM to 10 aM, were amplified by LAMP in the presence of nanoflowers. The FMR spectra of samples at the 15 min amplification end points were measured (Figure 5a, average spectra of three independent replicates). Additionally, four types of negative control NS5 gene from relevant viruses, i.e., Dengue virus, Yellow fever virus, Japanese encephalitis virus, and West Nile virus, were tested as well (spectra not shown). The concentration of negative control oligonucleotides was 100 fM. Blank controls (1× PBS containing 20% serum) were measured for normalizing B_{res} and for calculating the cutoff value. The increases of B_{res} after the LAMP reaction are shown in Figure 5b. The lowest target concentration with a ΔB_{res} above the cutoff value was 100 aM. A plateau of ΔB_{res} was observed at target concentrations of 10 and 100 fM. Responses from the negative controls are all below the cutoff value, indicating a high specificity of the proposed method. In a previous work we have demonstrated that *Bst* 3.0 polymerase was capable of amplifying both RNA and DNA sequences under identical conditions;[57] therefore, the proposed system can be directly extended for RNA detection.

Compared to the BNF-100 MNPs used in RCA-based biosensing, synomag-D nanoflowers exhibit a significantly smaller FMR peak-to-peak line width. In such cases, when the overlap between positive and negative spectral components are smaller, it becomes feasible to fit the intermediate spectra to a linear combination of positive and negative end point spectra: $c = aC_1 + bC_2$. Here, $C_1/(C_1 + C_2)$ corresponds to the fraction of rotationally free nanoflowers in the suspension. Although less direct, this method provides a quantitative and more precise measure than the determination of resonance field shifts (ΔB_{res}). Examples of data fitting using this approach are shown in Figure S3.

DOI: 10.1021/acssensors.8b00048
ACS Sens. 2018, 3, 1093−1101

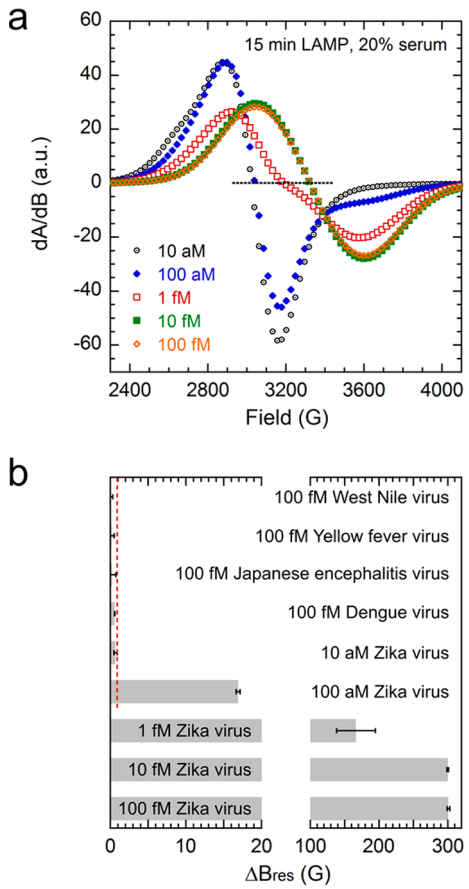

Figure 5. Dose response and specificity study of the LAMP-based FMR sensing. (a) FMR spectra of different concentrations of target DNA (ranging from 100 fM to 10 aM). The black dotted horizontal line indicates the zero value of dA/dB. (b) Resonance field shifts (ΔB_{res}). All the samples are prepared in 20% serum and measured after 15 min of LAMP. The red dashed vertical line indicates the cutoff value. Error bars indicate 1 standard deviation based on three independent measurements.

CONCLUSIONS

To summarize, we have demonstrated an FMR-based homogeneous and volumetric MNP sensing method for DNA detection. Combined with isothermal DNA amplification methods, the proposed biosensor can quantify the target DNA by monitoring the shift of the ferromagnetic resonance field (ΔB_{res}) of the suspension. Target analytes in a very small sample volume (10 μL) can be rapidly detected with high sensitivity and repeatability. For RCA-based biosensing, an LOD of 1 pM was demonstrated with a linear detection range of approximately 2 orders of magnitude. For LAMP-based sensing with nonfunctionalized magnetic nanoflowers, the sensitivity was demonstrated to be 100 aM for 20% serum samples. Future work on this biosensor system includes the design of miniaturized FMR sensor units, multiplexing of MNP labels, and real-time (kinetic) measurements.

ASSOCIATED CONTENT

Supporting Information

The Supporting Information is available free of charge on the ACS Publications website at DOI: 10.1021/acssensors.8b00048.

Sequences of templates and probes used for RCA-based biosensing; sequences of templates and primers used for LAMP-based sensing; MNP (BNF-100) concentration dependent FMR response curve; observation of BNF-100 chains in an optical microscope; Fitting of FMR-LAMP spectra using a linear combination approach (PDF)

AUTHOR INFORMATION

Corresponding Authors

*E-mail: mattias.stromberg@angstrom.uu.se.
*E-mail: erik.wetterskog@angstrom.uu.se.

ORCID

Bo Tian: 0000-0002-5249-4415
Mattias Strömberg: 0000-0003-0648-3130
Erik Wetterskog: 0000-0002-6681-4803

Notes

The authors declare no competing financial interest.

ACKNOWLEDGMENTS

The authors acknowledge financial support from Swedish Research Council Formas (Project no. 221-2012-444 and 2011-1692) and EU FP7 Grant No. FP7-NMP-604448. Fikret Mamedov is kindly acknowledged for technical support during the FMR measurements. Stefan Gustafsson at Chalmers University of Technology is acknowledged for acquisition of the TEM micrograph in Figure 1. Cordula Grüttner at micromod Partikeltechnologie GmbH is acknowledged for the kind provision of the Synomag-D samples.

REFERENCES

(1) Foy, C. A.; Parkes, H. C. Emerging homogeneous DNA-based technologies in the clinical laboratory. *Clin. Chem.* **2001**, *47*, 990−1000.

(2) Reynolds, R. A.; Mirkin, C. A.; Letsinger, R. L. Homogeneous, nanoparticle-based quantitative colorimetric detection of oligonucleotides. *J. Am. Chem. Soc.* **2000**, *122*, 3795−3796.

(3) Huang, X. L.; Liu, Y. J.; Yung, B.; Xiong, Y. H.; Chen, X. Y. Nanotechnology-Enhanced No-Wash Biosensors for in Vitro Diagnostics of Cancer. *ACS Nano* **2017**, *11*, 5238−5292.

(4) Issadore, D.; Park, Y. I.; Shao, H.; Min, C.; Lee, K.; Liong, M.; Weissleder, R.; Lee, H. Magnetic sensing technology for molecular analyses. *Lab Chip* **2014**, *14*, 2385−2397.

(5) Lee, H.; Shin, T. H.; Cheon, J.; Weissleder, R. Recent Developments in Magnetic Diagnostic Systems. *Chem. Rev.* **2015**, *115*, 10690−10724.

(6) Schrittwieser, S.; Pelaz, B.; Parak, W. J.; Lentijo-Mozo, S.; Soulantica, K.; Dieckhoff, J.; Ludwig, F.; Guenther, A.; Tschope, A.; Schotter, J. Homogeneous Biosensing Based on Magnetic Particle Labels. *Sensors* **2016**, *16*, 828.

(7) Lee, N.; Hyeon, T. Designed synthesis of uniformly sized iron oxide nanoparticles for efficient magnetic resonance imaging contrast agents. *Chem. Soc. Rev.* **2012**, *41*, 2575−2589.

(8) Goodwill, P. W.; Saritas, E. U.; Croft, L. R.; Kim, T. N.; Krishnan, K. M.; Schaffer, D. V.; Conolly, S. M. X-Space MPI: Magnetic Nanoparticles for Safe Medical Imaging. *Adv. Mater.* **2012**, *24*, 3870−3877.

(9) Huang, J.; Li, Y. C.; Orza, A.; Lu, Q.; Guo, P.; Wang, L. Y.; Yang, L.; Mao, H. Magnetic Nanoparticle Facilitated Drug Delivery for Cancer Therapy with Targeted and Image-Guided Approaches. *Adv. Funct. Mater.* **2016**, *26*, 3818−3836.

(10) Tong, S.; Quinto, C. A.; Zhang, L. L.; Mohindra, P.; Bao, G. Size-Dependent Heating of Magnetic Iron Oxide Nanoparticles. *ACS Nano* **2017**, *11*, 6808−6816.

DOI: 10.1021/acssensors.8b00048
ACS Sens. 2018, 3, 1093−1101

(11) Chemla, Y. R.; Crossman, H. L.; Poon, Y.; McDermott, R.; Stevens, R.; Alper, M. D.; Clarke, J. Ultrasensitive magnetic biosensor for homogeneous immunoassay. *Proc. Natl. Acad. Sci. U. S. A.* **2000**, *97*, 14268−14272.
(12) Grossman, H. L.; Myers, W. R.; Vreeland, V. J.; Bruehl, R.; Alper, M. D.; Bertozzi, C. R.; Clarke, J. Detection of bacteria in suspension by using a superconducting quantum interference device. *Proc. Natl. Acad. Sci. U. S. A.* **2004**, *101*, 129−134.
(13) Fornara, A.; Johansson, P.; Petersson, K.; Gustafsson, S.; Qin, J.; Olsson, E.; Ilver, D.; Krozer, A.; Muhammed, M.; Johansson, C. Tailored Magnetic Nanoparticles for Direct and Sensitive Detection of Biomolecules in Biological Samples. *Nano Lett.* **2008**, *8*, 3423−3428.
(14) Tian, B.; Qiu, Z.; Ma, J.; Zardán Gómez de la Torre, T.; Johansson, C.; Svedlindh, P.; Strömberg, M. Attomolar Zika virus oligonucleotide detection based on loop-mediated isothermal amplification and AC susceptometry. *Biosens. Bioelectron.* **2016**, *86*, 420−425.
(15) Kaittanis, C.; Naser, S. A.; Perez, J. M. One-step, nanoparticle-mediated bacterial detection with magnetic relaxation. *Nano Lett.* **2007**, *7*, 380−383.
(16) Chen, Y. P.; Xianyu, Y. L.; Wang, Y.; Zhang, X. Q.; Cha, R. T.; Sun, J. S.; Jiang, X. Y. One-Step Detection of Pathogens and Viruses: Combining Magnetic Relaxation Switching and Magnetic Separation. *ACS Nano* **2015**, *9*, 3184−3191.
(17) Park, S. Y.; Handa, H.; Sandhu, A. Magneto-Optical Biosensing Platform Based on Light Scattering from Self-Assembled Chains of Functionalized Rotating Magnetic Beads. *Nano Lett.* **2010**, *10*, 446−451.
(18) Tian, B.; Ma, J.; Qiu, Z.; Zardán Gómez de la Torre, T.; Donolato, M.; Hansen, M. F.; Svedlindh, P.; Strömberg, M. Optomagnetic Detection of MicroRNA Based on Duplex-Specific Nuclease-Assisted Target Recycling and Multilayer Core-Satellite Magnetic Superstructures. *ACS Nano* **2017**, *11*, 1798−1806.
(19) Smit, J.; Beljers, H. G. Ferromagnetic resonance absorption in BaFe12O19, a highly anisotropic crystal. *Philips Res. Rep.* **1955**, *10*, 31.
(20) Farle, M. Ferromagnetic resonance of ultrathin metallic layers. *Rep. Prog. Phys.* **1998**, *61*, 755−826.
(21) Raikher, Y. L.; Stepanov, V. I. The effect of thermal fluctuations on the FMR line shape in dispersed ferromagnets. *J. Exp. Theor. Phys.* **1992**, *102*, 1409−1423.
(22) Usselman, R. J.; Klem, M. T.; Russek, S. E.; Young, M.; Douglas, T.; Goldfarb, R. B. Two-component magnetic structure of iron oxide nanoparticles mineralized in Listeria innocua protein cages. *J. Appl. Phys.* **2010**, *107*, 114703.
(23) Winklhofer, M.; Chang, L.; Eder, S. H. K. On the magnetocrystalline anisotropy of greigite (Fe3S4). *Geochem., Geophys., Geosyst.* **2014**, *15*, 1558−1579.
(24) Kittel, C. On the Theory of Ferromagnetic Resonance Absorption. *Phys. Rev.* **1948**, *73*, 155−161.
(25) Charilaou, M.; Winklhofer, M.; Gehring, A. U. Simulation of ferromagnetic resonance spectra of linear chains of magnetite nanocrystals. *J. Appl. Phys.* **2011**, *109*, 093903.
(26) Raikher, Y. L.; Stepanov, V. I. Ferromagnetic-Resonance in a Suspension of Single-Domain Particles. *Phys. Rev. B: Condens. Matter Mater. Phys.* **1994**, *50*, 6250−6259.
(27) Gazeau, F.; Bacri, J. C.; Gendron, F.; Perzynski, R.; Raikher, Y. L.; Stepanov, V. I.; Dubois, E. Magnetic resonance of ferrite nanoparticles: evidence of surface effects. *J. Magn. Magn. Mater.* **1998**, *186*, 175−187.
(28) Usselman, R. J.; Russek, S. E.; Klem, M. T.; Allen, M. A.; Douglas, T.; Young, M.; Idzerda, Y. U.; Singel, D. J. Temperature dependence of electron magnetic resonance spectra of iron oxide nanoparticles mineralized in Listeria innocua protein cages. *J. Appl. Phys.* **2012**, *112*, 084701.
(29) Wetterskog, E.; Castro, A.; Zeng, L.; Petronis, S.; Heinke, D.; Olsson, E.; Nilsson, L.; Gehrke, N.; Svedlindh, P. Size and property bimodality in magnetic nanoparticle dispersions: single domain particles vs. strongly coupled nanoclusters. *Nanoscale* **2017**, *9*, 4227−4235.
(30) Wago, K.; Botkin, D.; Yannoni, C. S.; Rugar, D. Paramagnetic and ferromagnetic resonance imaging with a tip-on-cantilever magnetic resonance force microscope. *Appl. Phys. Lett.* **1998**, *72*, 2757−2759.
(31) Puzic, A.; Van Waeyenberge, B.; Chou, K. W.; Fischer, P.; Stoll, H.; Schutz, G.; Tyliszczak, T.; Rott, K.; Bruckl, H.; Reiss, G.; Neudecker, I.; Haug, T.; Buess, M.; Back, C. H. Spatially resolved ferromagnetic resonance: Imaging of ferromagnetic eigenmodes. *J. Appl. Phys.* **2005**, *97*, 10E704.
(32) Obukhov, Y.; Pelekhov, D. V.; Kim, J.; Banerjee, P.; Martin, I.; Nazaretski, E.; Movshovich, R.; An, S.; Gramila, T. J.; Batra, S.; Hammel, P. C. Local ferromagnetic resonance imaging with magnetic resonance force microscopy. *Phys. Rev. Lett.* **2008**, *100*, 197601.
(33) Lee, I.; Obukhov, Y.; Xiang, G.; Hauser, A.; Yang, F. Y.; Banerjee, P.; Pelekhov, D. V.; Hammel, P. C. Nanoscale scanning probe ferromagnetic resonance imaging using localized modes. *Nature* **2010**, *466*, 845−848.
(34) Ghionea, S.; Dhagat, P.; Jander, A. Ferromagnetic resonance detection for magnetic microbead sensors. *IEEE Sens. J.* **2008**, *8*, 896−902.
(35) Chatterjee, E.; Marr, T.; Dhagat, P.; Remcho, V. T. A microfluidic sensor based on ferromagnetic resonance induced in magnetic bead labels. *Sens. Actuators, B* **2011**, *156*, 651−656.
(36) Metaxas, P. J.; Sushruth, M.; Begley, R. A.; Ding, J.; Woodward, R. C.; Maksymov, I. S.; Albert, M.; Wang, W.; Fangohr, H.; Adeyeye, A. O.; Kostylev, M. Sensing magnetic nanoparticles using nano-confined ferromagnetic resonances in a magnonic crystal. *Appl. Phys. Lett.* **2015**, *106*, 232406.
(37) Sushruth, M.; Ding, J. J.; Duczynski, J.; Woodward, R. C.; Begley, R. A.; Fangohr, H.; Fuller, R. O.; Adeyeye, A. O.; Kostylev, M.; Metaxas, P. J. Resonance-Based Detection of Magnetic Nanoparticles and Microbeads Using Nanopatterned Ferromagnets. *Phys. Rev. Appl.* **2016**, *6*, 044005.
(38) Fock, J.; Jonasson, C.; Johansson, C.; Hansen, M. F. Characterization of fine particles using optomagnetic measurements. *Phys. Chem. Chem. Phys.* **2017**, *19*, 8802−8814.
(39) Osborn, J. A. Demagnetizing Factors of the General Ellipsoid. *Phys. Rev.* **1945**, *67*, 351−357.
(40) Ahrentorp, F.; Astalan, A.; Blomgren, J.; Jonasson, C.; Wetterskog, E.; Svedlindh, P.; Lak, A.; Ludwig, F.; Van IJzendoorn, L. J.; Westphal, F.; Gruettner, C.; Gehrke, N.; Gustafsson, S.; Olsson, E.; Johansson, C. Effective particle magnetic moment of multi-core particles. *J. Magn. Magn. Mater.* **2015**, *380*, 221−226.
(41) Saville, S. L.; Qi, B.; Baker, J.; Stone, R.; Camley, R. E.; Livesey, K. L.; Ye, L. F.; Crawford, T. M.; Mefford, O. T. The formation of linear aggregates in magnetic hyperthermia: Implications on specific absorption rate and magnetic anisotropy. *J. Colloid Interface Sci.* **2014**, *424*, 141−151.
(42) Faraudo, J.; Andreu, J. S.; Calero, C.; Camacho, J. Predicting the Self-Assembly of Superparamagnetic Colloids under Magnetic Fields. *Adv. Funct. Mater.* **2016**, *26*, 3837−3858.
(43) Tian, B.; Wetterskog, E.; Qiu, T.; Zardán Gómez de la Torre, T.; Donolato, M.; Hansen, M. F.; Svedlindh, P.; Strömberg, M. Shape anisotropy enhanced optomagnetic measurement for prostate-specific antigen detection via magnetic chain formation. *Biosens. Bioelectron.* **2017**, *98*, 285−291.
(44) Raikher, Y. L. The Magnetization Curve of a Textured Ferrofluid. *J. Magn. Magn. Mater.* **1983**, *39*, 11−13.
(45) Liu, D. Y.; Daubendiek, S. L.; Zillman, M. A.; Ryan, K.; Kool, E. T. Rolling circle DNA synthesis: Small circular oligonucleotides as efficient templates for DNA polymerases. *J. Am. Chem. Soc.* **1996**, *118*, 1587−1594.
(46) Ali, M. M.; Li, F.; Zhang, Z. Q.; Zhang, K. X.; Kang, D. K.; Ankrum, J. A.; Le, X. C.; Zhao, W. A. Rolling circle amplification: a versatile tool for chemical biology, materials science and medicine. *Chem. Soc. Rev.* **2014**, *43*, 3324−3341.
(47) Østerberg, F. W.; Rizzi, G.; Donolato, M.; Bejhed, R. S.; Mezger, A.; Strömberg, M.; Nilsson, M.; Strømme, M.; Svedlindh, P.; Hansen, M. F. On-Chip Detection of Rolling Circle Amplified DNA Molecules

DOI: 10.1021/acssensors.8b00048
ACS Sens. 2018, 3, 1093−1101

from Bacillus Globigii Spores and Vibrio Cholerae. *Small* **2014**, *10*, 2877−2882.
(48) Strömberg, M.; Goransson, J.; Gunnarsson, K.; Nilsson, M.; Svedlindh, P.; Strømme, M. Sensitive molecular diagnostics using volume-amplified magnetic nanobeads. *Nano Lett.* **2008**, *8*, 816−821.
(49) Zardán Gómez de la Torre, T.; Mezger, A.; Herthnek, D.; Johansson, C.; Svedlindh, P.; Nilsson, M.; Strømme, M. Detection of rolling circle amplified DNA molecules using probe-tagged magnetic nanobeads in a portable AC susceptometer. *Biosens. Bioelectron.* **2011**, *29*, 195−199.
(50) Donolato, M.; Antunes, P.; Bejhed, R. S.; Zardán Gómez de la Torre, T.; Østerberg, F. W.; Strömberg, M.; Nilsson, M.; Strømme, M.; Svedlindh, P.; Hansen, M. F.; Vavassori, P. Novel Readout Method for Molecular Diagnostic Assays Based on Optical Measurements of Magnetic Nanobead Dynamics. *Anal. Chem.* **2015**, *87*, 1622−1629.
(51) Pavuluri, S. K.; Lopez-Villarroya, R.; McKeever, E.; Goussetis, G.; Desmulliez, M. P. Y.; Kavanagh, D. Integrated Microfluidic Capillary in a Waveguide Resonator for Chemical and Biomedical Sensing. *J. Phys. Conf. Ser.* **2009**, *178*, 012009.
(52) Little, C. E.; Russek, S. E.; Booth, J. C.; Kabos, P.; Usselman, R. J. On-wafer magnetic resonance of magnetite nanoparticles. *J. Magn. Magn. Mater.* **2015**, *393*, 15−19.
(53) Banholzer, A.; Narkowicz, R.; Hassel, C.; Meckenstock, R.; Stienen, S.; Posth, O.; Suter, D.; Farle, M.; Lindner, J. Visualization of spin dynamics in single nanosized magnetic elements. *Nanotechnology* **2011**, *22*, 295713.
(54) Schoeppner, C.; Wagner, K.; Stienen, S.; Meckenstock, R.; Farle, M.; Narkowicz, R.; Suter, D.; Lindner, J. Angular dependent ferromagnetic resonance analysis in a single micron sized cobalt stripe. *J. Appl. Phys.* **2014**, *116*, 033913.
(55) Gavilan, H.; Kowalski, A.; Heinke, D.; Sugunan, A.; Sommertune, J.; Varon, M.; Bogart, L. K.; Posth, O.; Zeng, L. J.; Gonzalez-Alonso, D.; Balceris, C.; Fock, J.; Wetterskog, E.; Frandsen, C.; Gehrke, N.; Gruttner, C.; Fornara, A.; Ludwig, F.; Veintemillas-Verdaguer, S.; Johansson, C.; Morales, M. P. Colloidal Flower-Shaped Iron Oxide Nanoparticles: Synthesis Strategies and Coatings. *Part. Part. Syst. Char.* **2017**, *34*, 1700094.
(56) Bender, P.; Fock, J.; Frandsen, C.; Hansen, M. F.; Balceris, C.; Ludwig, F.; Posth, O.; Wetterskog, E.; Bogart, L. K.; Southern, P.; Szczerba, W.; Zeng, L. J.; Witte, K.; Gruttner, C.; Westphal, F.; Honecker, D.; Gonzalez-Alonso, D.; Barquin, L. F.; Johansson, C. Relating Magnetic Properties and High Hyperthermia Performance of Iron Oxide Nanoflowers. *J. Phys. Chem. C* **2018**, *122*, 3068−3077.
(57) Tian, B.; Ma, J.; Zardán Gómez de la Torre, T.; Balint, A.; Donolato, M.; Hansen, M. F.; Svedlindh, P.; Strömberg, M. Rapid Newcastle Disease Virus Detection Based on Loop-Mediated Isothermal Amplification and Optomagnetic Readout. *ACS Sens.* **2016**, *1*, 1228−1234.

DOI: 10.1021/acssensors.8b00048
ACS Sens. 2018, 3, 1093−1101